Chapter 6

Fluorescence guided Superparamagnetic g-C_3N_4@$FeNi_3$-heterostructure for cancer cell imaging and detection

Compared to existing organic compounds which have limited lifetime and low stability in biological environments, Fluorescence imaging materials has gained attention recently, due to its viable ways in detecting cancerous cells. Having its potential in providing high resolution images with enhanced contrast, and better diagnosis, fluorescence imaging has the ability of early detection of cancer for its most curable form. In this chapter, we have developed a superparamagnetic biocompatible g-C_3N_4@$FeNi_3$ heterostructure for sensitive and early detection of cancer under the direction of fluorescence imaging. The heterostructure was further evaluated, after it was functionalized with PEG to minimize nonspecific interactions with biomolecules in living cells. Hence, potential of this platform is to overcome the drawbacks of commercial fluorophores and enhance their merit of application as labels for optical imaging.

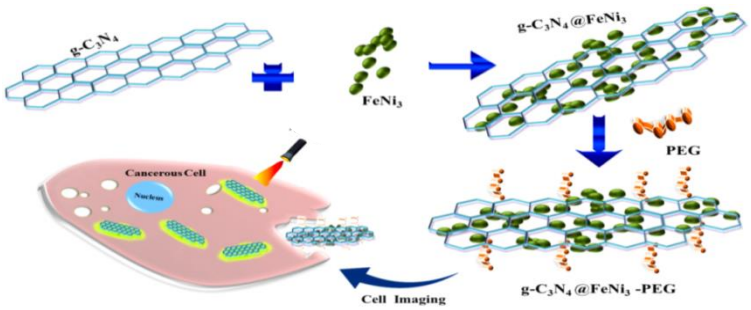

Figure 6.1: Schematic illustration of functionalization 2D heterostructure materials for targeted imaging of cancerous cells.

This portion of the thesis is published in M. Talukdar et al. *Materials Letters* ***333****, (2023), 2101943.*

6.1 Introduction:

Cancer is a major worldwide threat to human life as it can affect any organ or tissue of the human body. Modern treatment procedures such as radiation and chemo therapies are used to cure such type of diseases [1,2]. Recently, non-invasive Phototherapy approaches including photothermal therapy (PTT) and photodynamic therapy (PDT) have attracted wide-ranging interest owing to its flexibility of treatment which is activated by light [3-5]. But in order to undergo such treatments, early diagnosis of the disease is required. Fluorescence imaging has aided as a proficient technique that offers real-time contrast improvement in the operating area for monitoring tumor cells [6-9]. Several fluorescent dyes such as porphyrin, cyanine, Rhodamine, Alexa Fluor 405, fluorescein, etc. have been recognized as potential fluorophores for improved fluorescence imaging [10]. To overcome the aforementioned obstructions, quantum dot (QDs) nanomaterials [11-14] are also used, which have the advantage of high quantum yield, offering enhanced brightness over ordinary organic fluorophores. QDs are excellent probes for bioimaging applications, but one of its major drawbacks is their blinking behaviour, in which dark periods of no emission interrupt fluorescence for longer period. It also has few disadvantages which are not helpful for signal acquisition. Disparity and water solubility of these quantum dots must be ensured with appropriate synthesis routes for its better applicability. Finally, due to high toxicity, this can pose as a potential risk to the human health for which their use in medical application is restricted. But materials providing more specific cancer treatments without undesired side effects can be good allies for accurate diagnosis and successful therapies. In consideration of the inherent intricacies of cancer, a nanocarrier as a delivery vehicle is no longer enough to achieve the obligations of dealing with cancer. It is extremely important to track the dynamic route of the nanocarrier, so that their action inside the organism can be precisely recognized. In this regard, the delivery system with fluorescent properties seems to be an attractive choice for cancer treatment. Two dimensional (2D) biocompatible nanomaterials with tunable

functionalities have opened the door for addressing current challenges, related to clinical treatment of cancer therapy [15-18]. 2D materials due to its versatile physicochemical properties have empowered a new horizon for applications in biomedical. Large surface area 2D materials can have diverse applications in cancer therapies. Advantages of 2D C-N planes along with pi-conjugated electronic structures make them suitable for fluorescence emission. Also, due to large extinction coefficient, these 2D materials offer efficient capabilities in photo thermal conversion and deep tissue penetration. Prior literatures have established its use in diverse aspects, due to its propensity towards tumor cells, molecular imaging, PDT and PTT therapies. But it has easy tendency to accumulate or aggregate, which results *in vivo* toxicity, and slow metabolism causing toxicity in main organs. Due to exponential growth of two dimensional materials in biomedical application, it is an unmet challenge to improve the biocompatibility and cytotoxicity assays of these materials with proper optimized concentration. Also, most of the literatures focus on boosting the antimicrobial properties of such developed systems, but the undesirable consequences like cytotoxicity increment are completely overlooked. However, developing strategies such as building heterostructures helps in fine-tuning of their synergistic physicochemical properties and biological effects, which further aids in enhancing the therapy efficiency. Tuning the band structure of 2D nanomaterial further helps in improving its sensitivity towards light absorbance in broad spectra. Graphitic carbon nitride (g-C_3N_4), due to its enhanced intrinsic blue fluorescence, low toxicity, wide and controllable band gap has attained tremendous attention in water purification as a catalyst [19-22]. In this work, pristine nanomaterials combined with other material to form heterostructure have been explored intensively in biomedical applications due to its advantageous properties. To improve the tunable emission and electronic properties of pristine g-C_3N_4, it is conjugated with 1D iron-nickel nanoparticles to form a heterostructure, providing additional active sites with modified local chemical activities of g-C_3N_4. 1D $FeNi_3$ nanochain is added into the g-C_3N_4 sheets which not only helped in enhancing the

photoresponsive range, but is also beneficial as, it has long circulation time in blood stream for therapeutic applications. Moreover, advantages of superparamagnetic heterostructure were chosen over other materials for cell labelling purposes. These systems are effectively taken up and do not have any negative effect on the viability of cells. Because of higher hysteresis losses for one-domain magnetic particles, superparamagnetic generate more heat compared to ferromagnetic materials under the same conditions. The heat that is released leads to adjuvant treatment for chemotherapy or radiotherapy. Further, a layer of bio-compatible hydrophilic polymer, such as poly(ethylene glycol) (PEG), is further engrafted onto the surface of the heterostructure, as this polymer prevents the heterostructure from nonspecific adsorption of biomolecules when injected inside the body. Biocompatibility of developed heterostructure was further evaluated which showed no significant change in their viability from 10μM to 500μM concentration. Also, confocal fluorescence microscopy in living cancer cells confirmed its potential application as labels for optical imaging. The aforementioned heterostructure with fluorescence imaging capability will be used to track and target the specific cancer cell, adding accurate interpretation of the cell. The reported paradigm with abundant surface chemistry, high photoluminescence (PL), excellent physiological stability, low toxicity and fluorescence imaging will help in ensuring its efficiency as a contrast probe.

6.2. Methodology

6.2.1. Experimental Details:

6.2.1.1 Chemicals and materials used

Precursors like, Urea (CH_4N_2O), Ethanol (C_2H_6O), Diphenyl ether ($C_{12}H_{10}O$), Hydrazine (N_2H_4), Ethylene glycol ($C_2H_6O_2$), Sodium Acetate ($C_2H_3NaO_2$), Ferric chloride ($FeCl_3$), Nickel chloride hexahydrate($NiCl_26H_2O$), chemicals with 99.97% purity from Merck were used during synthesis. Double distilled water was used for washing purposes during the synthesis process. Polyethylene glycol (PEG) and

isopropanol were utilized for PEGylation process. The experiments were repeated for three times to achieve the uncertainties in the results.

6.2.1.2. Development of g-C_3N_4@$FeNi_3$ nanocomposite: Individual preparation of g-C_3N_4 and $FeNi_3$ was carried out, which was conducted in our previous work, chapter number 2. In order to synthesize g-C_3N_4@$FeNi_3$ nanocomposite, g-C_3N_4 and $FeNi_3$ were mixed in distilled water separately with 2:1 (g-C_3N_4:$FeNi_3$) ratio. Then NaOH was added slowly to the resultant $FeNi_3$ solution maintaining the pH. After keeping both the individual under stirring, $FeNi_3$ was added drop wise into g-C_3N_4 solution. Later on, complete solution was centrifuged and washed with ethanol. Finally, the remaining precipitate was collected and dried at 70^0C for 8h so as to remove the water percentage. Ultimately, the collected dried samples are characterized respectively.

6.2.1.3. PEG functionalized g-C_3N_4@$FeNi_3$ nanocomposite:

In order to enhance the stability of the developed nanocomposite in solutions, it was engineered with hydrophilic PEG functional group which was conjugated to g-C_3N_4@$FeNi_3$ heterostructure by a noncovalent association. For that, 5 mg of the aforementioned prepared g-C_3N_4@$FeNi_3$ nanocomposite along with 50 mg of PEG (mW~ 4,000) were added with 10 mL of isopropanol. Later, the mixture was heated up to 100^0C for 3 hours under reflux condition to load PEG. Finally, the reaction mixture was cooled to room temperature where isopropanol gets evaporated. The remaining product was extracted, washed with ethanol and centrifuged. The final product was dried at 80^0C for 24hr. Once the product gets dried, all the experimental characterizations were carried out using the collected sample.

6.2.2. Biological assays:

6.2.2.1. Cell culture: Human breast cancer cell lines MCF-7 (luminal A subtype) and human embryonic kidney cells (HEK293) were cultured in Dulbecco's Modified

Essential Medium/ Ham's F-12 Medium (DMEM/F12) and DMEM media (HiMedia, India) supplemented with 10% fetal bovine serum (FBS) (Gibco, USA), respectively. All the cells were maintained at 37^0C with 5% carbon dioxide (CO2) in a humidified chamber. Cell lines were procured from ATCC and authenticated by STR profiling.

6.2.2.2. Cytotoxicity assays: Both breast cancer and normal human embryonic kidney and were treated with 10-500µM concentrations of the g-C_3N_4@$FeNi_3$ nanocomposite along with 5µg/ml of mitomycin as positive control. After 48 hours, 3-(4,5-dimethylthiazol-2-yl)-2,5-diphenyltetrazolium bromide (MTT) reagent was added at 5mg/ml concentration and incubated for 4 hours. Finally, absorbance of formed formazan crystals was measured at 570 and 630nm using Varioskan Flash reader (Thermo Fisher Scientific, USA) and percentage viability was calculated by normalizing the absorbance of treated group to untreated group.

6.2.2.3. *In vitro* nanocomposite characterization: Breast cancer MCF-7 cells were treated with 500µM concentration of g-C_3N_4@$FeNi_3$ nanocomposite for 48 hours. After 48 hours, cells were washed with the PBS and fluorescent spectra were measured at excitation wavelengths from 300-420nm using Varioskan Flash reader (Thermo Fisher Scientific, USA) at 20nm intervals.

6.2.2.4. Confocal microscopy imaging of g-C_3N_4@$FeNi_3$: MCF-7 cells were grown on a sterile coverslip and treated with the nanocomposite at 500µM concentration for 48 hours. The cells were fixed using 4% paraformaldehyde for 10 minutes and rinsed with PBS three times. Fixed cells were mounted on a glass slide using mowiol mounting solution (Sigma, USA). The fluorescent images were captured using DMi8 confocal microscope on Leica TCS SP8 platform (Leica Microsystems, Germany), excited at 405, 488 and 561nm wavelengths.

6.3 Results and Discussions:

6.3.1 Microstructural and Morphology

Due to low-toxicity and biocompatibility, 2D g-C_3N_4 nanosheets have been studied for cancer diagnosis and therapy. In this work, for the first time, 2D g-C_3N_4 has been conjugated with $FeNi_3$ nanoparticles to achieve high efficacy and induce multifunctionality in detecting cancerous cells. The major limitation was the short range in emission wavelength of g-C_3N_4. Herein, we have conjugated g-C_3N_4 with $FeNi_3$, where presence of Iron-Nickel alloy improved the heterostructure by enabling large absorption band, overlapping with g-C_3N_4 spectrum. **Figure 6.1** illustrates the schematic representation where $FeNi_3$ nanoparticles are distributed over 2D sheets and surface engineered with PEG to improve its stability. **Figure 6.2** (**a**) shows the micro-structural study of the heterostructure, which was carried out through x-ray diffraction. The diffraction peaks observed for the $FeNi_3$ nanoparticles were indexed as (111), (200) and (220) lattice plane reflections respectively, indicating face-centered cubic structure (JCPDS card No. 38-0419) [23]. In case of the graphitic carbon nitride, the peak at 27.4^0 corresponds to the lattice plane (002) (JCPDS card No. 87-1526) [24]. **Figure 6.2** (**b- d**) explicitly reveals the morphology of developed g-C_3N_4@$FeNi_3$ nanocomposite where g-C_3N_4 sheets are in layered distribution stacked together. Moreover, sheets are wrinkled and relatively flat having pores. **Figure 6.2** (**c and d**), further confirms that the developed $FeNi_3$ nanoparticles are decorated above the sheets having diameter around 80-100nm. Interestingly, $FeNi_3$ nanoparticles are distributed over the 2D sheet without blocking the pores of sheet. **Figure 6.2** (**e and f**) identifies the phase and topology profile of the system. Although $FeNi_3$ nanoparticles were present in the composite, surface roughness of the developed composite was negligible, which implies that no aggregation had occurred within the system after implementing $FeNi_3$ nanoparticles on g-C_3N_4 (which can further be justified from FESEM images). Moreover, smooth surface will be beneficial in treating the cancerous cells. Smooth surface of heterostructure will exhibit greater cellular uptake and more efficient access to degrade the disease site.

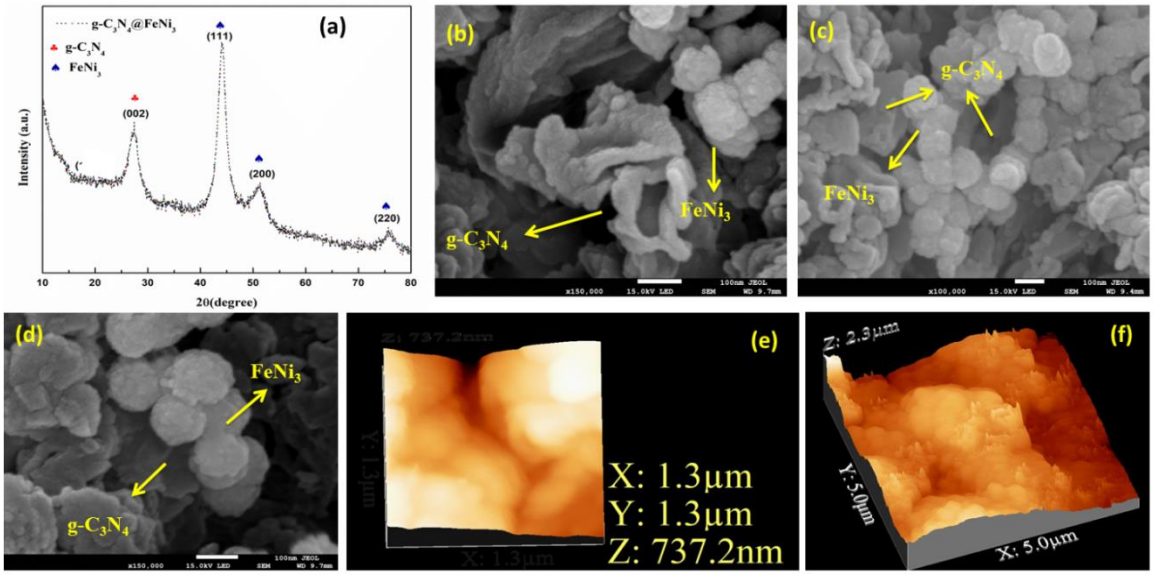

Figure 6.2: X-ray diffraction (XRD) patterns of g-C_3N_4@$FeNi_3$ heterostructure, FESEM images of g-C_3N_4@$FeNi_3$ heterostructure, AFM image of the developed heterostructure, where (d) indicates the topology (e) denotes the phase profile and (f) indicates the height of the heterostructure system.

6.3.2 Magnetic Property:

Since g-C_3N_4 and $FeNi_3$ materials energetically favour spin polarized ground states [26-27], it is exciting to investigate their magnetic properties. The heterostructure consisting carbon nitride and iron-nickel alloy systems exhibit magnetic hysteresis with superparamagnetic behaviour favouring its applicability in biomedical applications. Magnetization curves of g-C_3N_4@$FeNi_3$ heterostructure at 5 K, 150 K and 300 K temperature are shown in the **Figure 6.3 (a and b)**. The M-H hysteresis loop at room temperature shows the characteristics of superparamagnetism and hence there is no possibility of spin coupling in that condition. The coercivity values of the developed system are quite negligible and retentivity at 5 K, 150 K and 300 K are 6.07 emu/g, 4.06 emu/g and 4.03 emu/g respectively. Moreover, blocking temperature calculated at 100 Oe is found to be 38 K. It is worthwhile to note that there is no appearance of blocking temperature in ZFC curve in case of pristine g-

C_3N_4 [25]. Therefore, it clearly reveals that there is no ferromagnetic cluster behaviour in pristine g-C_3N_4 form. However, during the development of heterostructure, blocking temperature was found to be around 38 K.

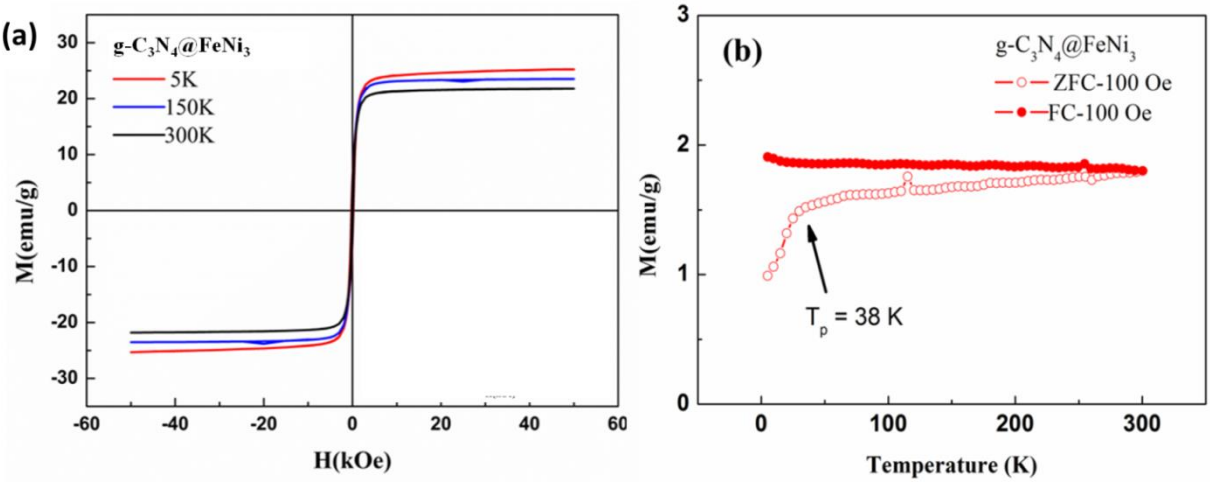

Figure 6.3: (a) Magnetic hysteresis curves of M-H plots for Hc and Mr measurements (b) Zero field cooled (ZFC) and field cooled (FC) magnetization curves of the heterostructure.

6.3.4 UV and PL Analysis

Figure 6.4 (**a**) shows the UV analysis of the heterostructure, showing a tail that covers the broad range of optical spectra from UV to the near-infrared region, resulting due to presence of Iron-nickel nanoparticles. The UV-vis absorption studies of samples before and after PEG functionalization shows a drop in intensity of absorption maxima. Also, the maxima have been observed to be red-shifted, inferring the interaction of PEG components with the 2D sheets and $FeNi_3$ nanoparticles. As ultraviolet light (UV, 320-420 nm), visible light (Vis, 420-760 nm), and near infrared light ranges lies beyond 1000 nm, the current study confirms that the system has extremely broad spectrum of absorbance, opening its wide application in PDT and PTT therapy [28]. Carbon nitride has absorption edge that response to UV light, [29] but presence of $FeNi_3$ has a significant absorption,

enhancing the Vis-NIR region and covering ultraviolet-visible-near infrared (UV-Vis-NIR) wavelength. Moreover, the 2D sheets have a large distribution of pore size structures and hence it can be concluded that all the UV-Vis-NIR light could be effectively absorbed and scattered within the pores.

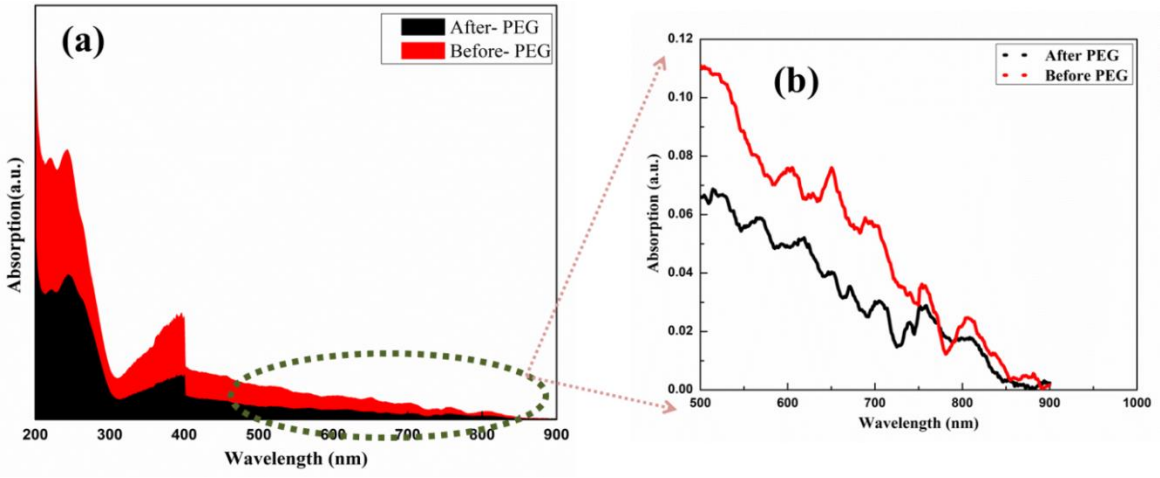

Figure 6.4: UV-vis spectra of g-C_3N_4@$FeNi_3$ heterostructure before and after pegylation in water solution.

Figure 6.5 shows the photoluminescence spectra of before and after PEG heterosystems at 358 nm excitation wavelength. The heterosystem indicates a broad emission peak at 435 nm. PEG acts as an energy acceptor which quenches the predicted fluorescence of the heterostructure. Thus, a reduction of the photoluminescence intensity could be observed in the after PEG heterosystem compared to the before PEG heterosystem. Modifying the bare system with PEG, quenches the inherent photoluminescence properties due to recombination of photogenerated electron-hole pairs in the overall heterostructure [30]. Since no spectral overlap was observed, so it can be concluded that the quenching occurred was due to electron transfer between the system and the PEG coating.

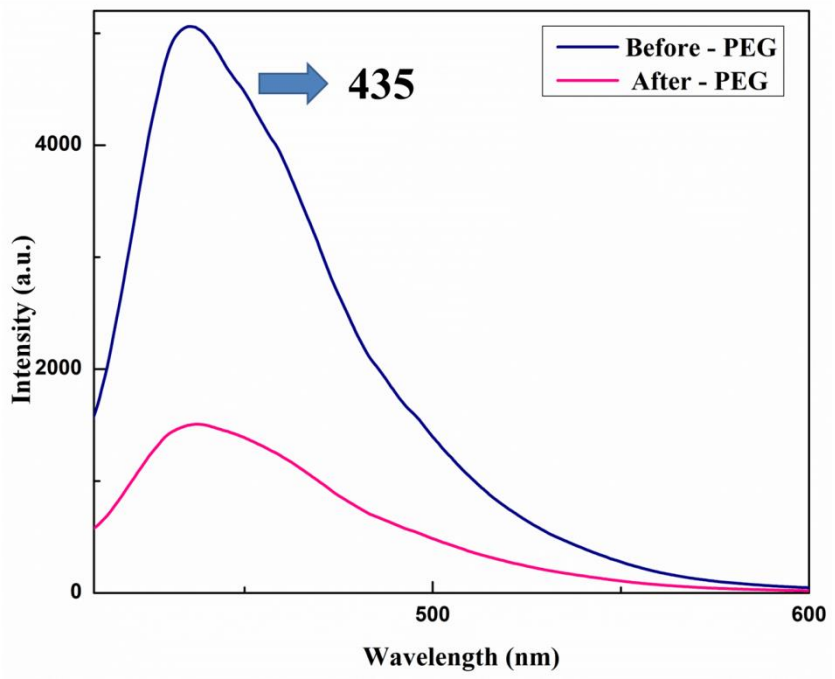

Figure 6.5: Photoluminescence emission spectra of g-C_3N_4@$FeNi_3$ heterostructure before and after pegylation in water solution.

6.3.5 Thermal and Surface charge Analysis

Figure 6.6 represents the TGA curve of before and after pegylation of the developed heterosystem. The PEGylated heterostructure appeared to degrade at a temperature of 600^0C. It is clearly evident that due to the grafted polymer in the heterostructure, more energy is needed to cleave the bond between the nanomaterials for which the sample after pegylation degrades at higher temperature. Moreover, the PEG grafting percentage relative to the whole g-C_3N_4@$FeNi_3$ heterostructure was estimated to be 1.19 wt %.

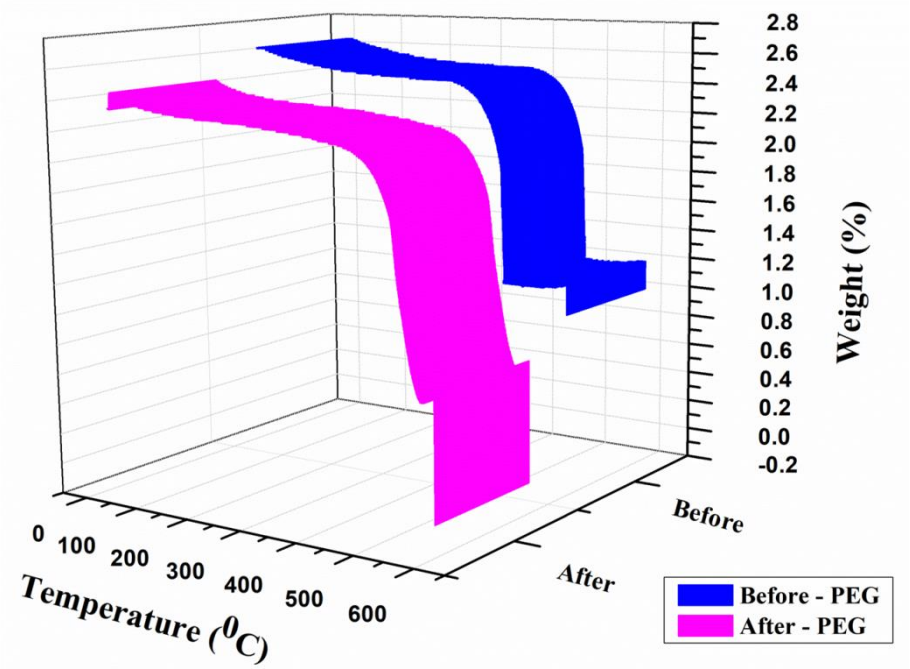

Figure 6.6: TGA of g-C_3N_4@$FeNi_3$ heterostructure.

Zeta potential study was performed in order to reveal the stability of the heterostructure system. Zeta-potential measurements were carried out for before and after PEGylation samples and the results are summarized in **Figure 6.7.** Formation of a thin PEG layer on the surface of the heterostructure lowers the zeta potential value from 7 mV to -7 mV at pH 7. This decrease in zeta potential value may be due to coverage of the heterostructure surface reactive groups with some negatively charged carboxylic acid groups [31]. Thus, decrease in Zeta potential further confirms the successful coating of PEG into the heterostructure system.

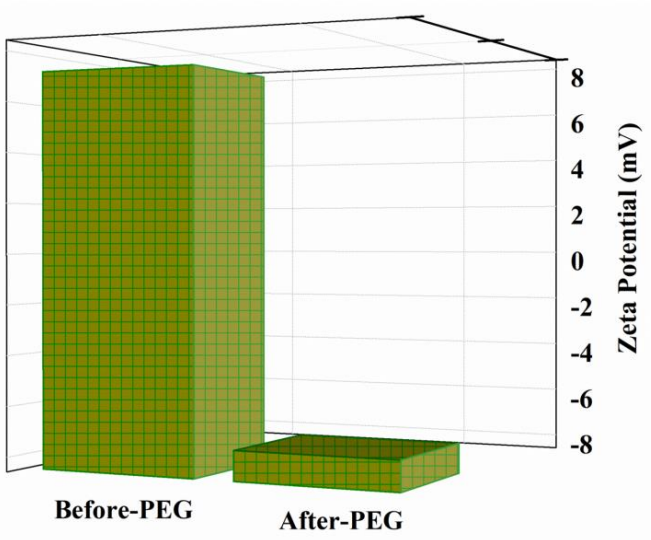

Figure 6.7: Zeta Potential distribution of g-C_3N_4@$FeNi_3$ heterostructure before and after pegylation in water solution.

6.3.6 Biological properties:

In order to analyse the biological properties of the nanocomposite and measure the optimum concentration, we performed cytotoxicity assay in human cell lines. Both Human Embryonic Kidney cell line (HEK293) and human breast cancer cell line (MCF-7) showed no significant change in their viability from 10μM to 500μM concentration, compared to positive control mitomycin (**Figure 6.8 a**). The highest concentration 500μM was selected for the *in vitro* nanocomposite fluorescence characterization to study the fluorescent excitation and emission spectra. MCF-7 breast cancer cell lines treated with the nanocomposite showed the excitation fluorescence wavelength at 400nm in the UV light spectra and peak emission spectra at 420nm (**Figure 6.8 b**). Following the *in vitro* nanocomposite characterization, we performed confocal fluorescence imaging analysis to study the cell permeability and nanocomposite intake and distribution inside the cells. MCF-7 cells treated with the nanocomposite were excited with UV laser at 405nm, green visible light laser at 488nm, and red visible light laser at 561nm. Interestingly, we observed significant cell permeability as well as cellular intake and distribution pattern in the cells upon excitation at 405nm (**Figure 6.9 a-c**). Broad emission spectra were observed between

518nm to 570nm in the visible spectral range and drastic reduction in the emission from 585nm to 650nm (**Figure 6.9 d-f**). **Figure 6.9** (**g-i**) showed the accumulation of nanocomposite significantly in the cytoplasmic region of MCF-7 cells.

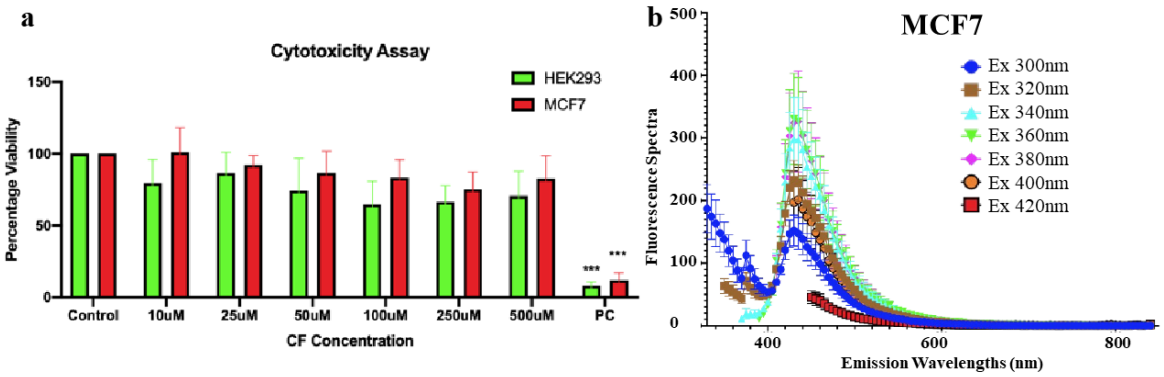

Figure 6.8: (a) Cytotoxicity assay for g-C_3N_4@$FeNi_3$ nanocomposite in human normal and cancer cell lines, (b) *in vitro* fluorescence characterization of g-C_3N_4@$FeNi_3$ nanocomposite.

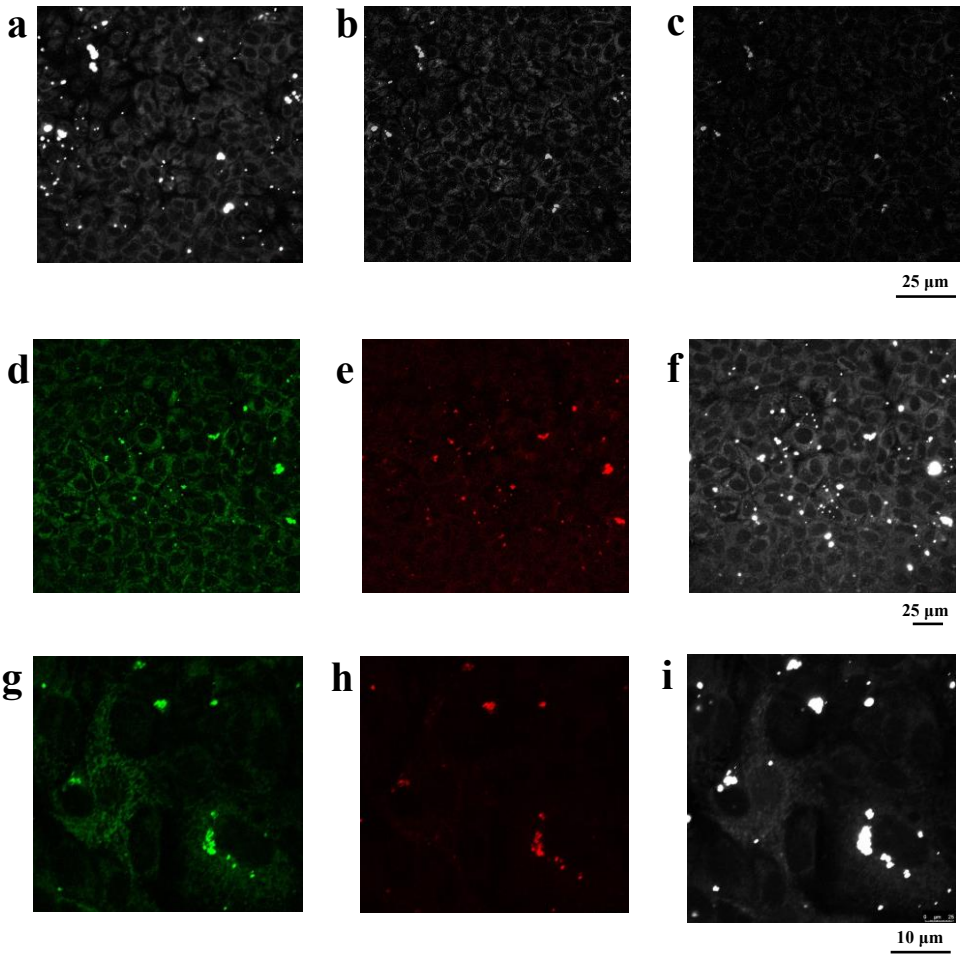

Figure 6.9: Confocal fluorescence imaging of g-C_3N_4@$FeNi_3$ nanocomposite treated MCF-7 cells (a) Ex: 405nm and Em: 420-750nm; (b) Ex: 405nm and Em: 420-600nm; (c) Ex: 405nm and Em: 600-750nm; (d) Ex: 488nm and Em: 518-570nm; (e) Ex: 561nm and Em: 585-650nm; (f) Ex: 405nm and Em: 420-750nm; zoomed in images of selected ROIs: (g) Ex: 488nm and Em: 518-570nm; (h) Ex: 561nm and Em: 585-650nm; and (i) Ex: 405nm and Em: 420-600nm.

6.4 Conclusion

Fluorescence imaging has emerged as biological imaging technology for tumor diagnosis, real-time monitoring of drug release and cancer therapy. In summary, this work reports on the integration of 2D g-C_3N_4 nanosheets with $FeNi_3$

nanoparticles for sensitive and specific identification of cancer cells through enhancing the contrast in fluorescence imaging property. Based on the conductivity of carbon nitride, with separation of electrons (e-) and holes (h+), and avoiding its recombination, the developed heterostructure can easily detect the cancerous cells with its inherent fluorescent imaging capability. Moreover, $FeNi_3$ nanoparticles with excellent magnetic targeted ability, when cladded with g-C_3N_4 acts as photosensitive agent helping to ablate the malignant cancer with no obvious side effects during the process of detection. Further, the resultant heterostructure showed superparamagnetic behaviour, which can be easily guided to the desired location simply with an external magnetic field. The bio distribution of heterostructure, along with cellular uptake inside the cells was also evaluated. In addition to their effectiveness as an alternate to pervasive organic dyes, the PEG functionalized heterostructure display good dispersion and biocompatibility leading towards a potential candidate for cell imaging assays. Due to its efficient versatility and non-toxicity, the developed heterostructure shows to be potential candidate as a synthetic platform for fluorescence imaging.

References

[1] Nigro, J. M., Baker, S. J., Preisinger, A. C., Jessup, J. M., Hostetter, R., Cleary, K., Bigner, S. H., Davidson, N., Baylin, S., Devilee, P., Glover, T., Collins, Francis S., Weston, A., Modali, R., Harris, C. C., and Vogelstein, Bert. Mutations in the p53 gene occur in diverse human tumour types. *Nature,* 342(6250):705-8, 1989.

[2] Bray, F., Ferlay, J., Soerjomataram, I., Siegel, R. L., Torre, L. A., and Jemal, A. Global cancer statistics 2018: GLOBOCAN estimates of incidence and mortality worldwide for 36 cancers in 185 countries. *CA: A Cancer Journal for Clinicians,* 68(6):394-424, 2018.

[3] Xu, X., Wu, H., Yang, Y., Liu, B., Tian, J., Bao H., and Liu, T. PLGA-coated methylene blue nanoparticles for photoacoustic imaging and photodynamic/photothermal cascaded precisely synergistic therapy of tumor. *RSC Advances*, 12:1543-1549, 2022.

[4] Liu, R., Gao, Y., Liu, N., and Suo, Y. Nanoparticles loading porphyrin sensitizers in improvement of photodynamic therapy for ovarian cancer. *Photodiagnosis and Photodynamic Therapy,* 33:102156-102174, 2021.

[5] Hong, L., Li, J., Luo, Y., Guo, T., Zhang, C., Ou, S., Long, Y., and Hu, Z. Recent Advances in Strategies for Addressing Hypoxia in Tumor Photodynamic Therapy. *Biomolecules,* 12(1):81-107, 2022.

[6] Cao, H., Qi, W., Gao, X., Wu, Q., Tian, L., and Wu, W. Graphene Quantum Dots prepared by Electron Beam Irradiation for Safe Fluorescence Imaging of Tumor. *Nanotheranostics*, 6(2):205-214, 2022.

[7] Campbell, E., Hasan, Md. T., Rodriguez, R. G., Akkaraju, G. R., and Naumov, A. V. Doped Graphene Quantum Dots for Intracellular Multicolor Imaging and Cancer Detection. *ACS Biomaterials Science & Engineering,* 5:4671-4682, 2019.

[8] Kumar, Y. R., Deshmukh, K., Sadasivuni, K. K., and Pasha, S. K. K. Graphene quantum dot based materials for sensing, bio-imaging and energy storage applications: a review. *RSC Advances,* 10:23861-23898, 2020.

[9] Sun, L., Xiong, Z., Shen, F., Wang, Z., and Liu, Z. Biological membrane derived nanomedicines for cancer therapy. *Science China Chemistry,* 64:719-733, 2021.

[10] Exner, R. M., Fernando C. C. T., and Pascu, S. Explorations into the Effect of meso-Substituents in Tricarbocyanine Dyes: A Path to Diverse Biomolecular Probes and Materials. *Angewandte Chemie,* 59:2-14, 2020.

[11] Singh, H., Sreedharan, S., Tiwari, K., Green, N. H., Smythe, C., Pramanik, S. K., Thomas, J. A., and Das, A. Two photon excitable graphene quantum dots for structured illumination microscopy and imaging applications: lysosome specificity and tissue-dependent imaging. *Chemical Communications,* 55:521-524, 2019.

[12] Wang, Z., Chen, D., Gu, B., Gao, B., Liu, Z., Yang, Y., Guo, Q., Zheng, X., and Wang, G. Yellow emissive nitrogen-doped graphene quantum dots as a label-free fluorescent probe for Fe^{3+} sensing and bioimaging. *Diamond and Related Materials,* 104:107749-107758, 2020.

[13] Columbus, S., Painuly, D., Nair, R. P., and Krishnan, V. K. Role of PEGylated CdSe-ZnS quantum dots on structural and functional properties of electrospun polycaprolactone scaffolds for blood vessel tissue engineering. *European Polymer Journal,* 151:110430-110438, 2021.

[14] Wang, X., Wu, X., Lu, Z., and Tao, X. Comparative Study of Time-Resolved Fluorescent Nanobeads, Quantum Dot Nanobeads and Quantum Dots as Labels in Fluorescence Immunochromatography for Detection of Aflatoxin B1 in Grains. *Biomolecules,* 10:575-587, 2020.

[15] Thiruppathi, R., Mishra, S., Ganapathy, M., Padmanabhan, P., and Gulyás, B. Nanoparticle Functionalization and Its Potentials for Molecular Imaging. *Advanced Science,* 4:1600279-1600293, 2017.

[16] Tyson, J. A., Mirabello, V., Calatayud, D. G., Ge, H., Kociok Köhn, G., Botchway, S. W., Pantoş, G. D., and Pascu, S. I. Thermally Reduced Graphene Oxide Nanohybrids of Chiral Functional Naphthalenediimides for Prostate Cancer Cells Bioimaging. *Advanced Functional Materials,* 26 (31):5641-5657, 2016.

[17] Naguib, M., Kurtoglu, M., Presser, V., Lu, J., Niu, J., Heon, M., Hultman, L., Gogotsi, Y., and Barsoum, M.-W. Two-Dimensional Nanocrystals Produced by Exfoliation of Ti_3AlC_2. *Advanced Materials*, 23:4248-4253, 2011.

[18] Lin, H., Wang, X., Yu, L. Chen, Y., and Shi, J. Two-Dimensional Ultrathin MXene Ceramic Nanosheets for Photothermal Conversion. *Nano Letters,* 17:384-391, 2017.

[19] Talukdar, M., Behera, S. K., Jana, S., Samal, P., and Deb, P. Band Alignment at Heterointerface with Rapid Charge Transfer Supporting Excellent Photocatalytic Degradation of Methylene Blue under Sunlight. *Advanced Materials Interfaces*, 9 (7):2101943-2101956, 2022.

[20] Talukdar, M., and Deb, P. Recent progress in research on multifunctional graphitic carbon nitride: An emerging wonder material beyond catalyst. *Carbon,* 192:308-331, 2022.

[21] Zhang, Z., Xu, R., Wang, Z., Dong, M., Cui, B., and Chen, M. Visible-Light Neural Stimulation on Graphitic-Carbon Nitride/Graphene Photocatalytic Fibers. *ACS Applied Materials & Interfaces,* 9:34736-34743, 2017.

[22] Talukdar, M., Nath, O., and Deb, P. Enhancing barrier properties of biodegradable film by reinforcing with 2D heterostructure. *Applied Surface Science,* 541:148464-148473, 2021.

[23] Talukdar, M., Behera, S. K., Bhattacharya, K., and Deb, P. Surface modified mesoporous g-C_3N_4@$FeNi_3$ as prompt and proficient magnetic adsorbent for crude oil recovery. *Applied Surface Science,* 473:275-281, 2019.

[24] Talukdar, M., Behera, S. K., and Deb, P. Graphitic carbon nitride decorated with $FeNi_3$ nanoparticles for flexible planar micro-supercapacitor with ultrahigh energy density and quantum storage capacity. *Dalton Transactions*, 48:12137-12146, 2019.

[25] Xu, K., Li, X., Chen, P., Zhou, D., Wu, C., Guo, Y., Zhang, L., Zhao, J., Wua, X., and Xie, Y. Hydrogen dangling bonds induce ferromagnetism in two-dimensional metal-free graphitic-C_3N_4 nanosheets. *Chemical Science,* 6(1):283-287, 2015.

[26] Gao, D., Liu, Y., Liu, P., Si, M., and Xue, D. Atomically Thin B doped g-C_3N_4 Nanosheets: High-Temperature Ferromagnetism and calculated Half-Metallicity. *Scientific Reports,* 6:35768-35776, 2016.

[27] Krasovskii, A.E. ELASTIC AND THERMAL PROPERTIES OF $FeNi_3$ ALLOYUNDER EARTH'S INNER CORE CONDITIONS. *Ukrainian Journal of Physics,* 50(8):0503-1265, 2005.

[28] Xu, W., Qian, J., Hou, G., Wang, Y., Wang, J., Sun, T., Ji, L., Suo, A., and Yao, Y. A dual-targeted hyaluronic acid-gold nanorod platform with triple-stimuli responsiveness for photodynamic/photothermal therapy of breast cancer. *Acta Biomaterialia,* 83:400-413, 2019.

[29] Zhuo, Z., Jiao, Y., Chen, L., Li, H., Dai, M., Lin, Z., Yang, H., Fu, F., and Dong, Y. Ultra-high quantum yield ultraviolet fluorescence of graphitic carbon nitride nanosheets. *Chemical Communications*, 55:15065-15068, 2019.

[30] Xiao, F., Gao, H., Lei, Y., Dai, W., Liu, M., Zheng, X., Cai, Z., Huang, X., Wu, H., and Ding, D. Guest-host doped strategy for constructing ultralong-lifetime near-infrared organic phosphorescence materials for bioimaging. *Nature Communications,* 13:186-196, 2022.

[31] Swartzwelter, B. J., Mayall, C., Alijagic, A., Barbero, F., Ferrari, E., Hernadi, S., Michelini, S., Pacheco, N. I. N., Prinelli, A., Swart, E., and Auguste, M. Cross-Species Comparisons of Nanoparticle Interactions with Innate Immune Systems: A Methodological Review. *Nanomaterials (Basel),* 11(6):1528-1560, 2021.